

Calcium carbonate nucleation driven by ion binding in a biomimetic matrix revealed by *in situ* electron microscopy

Paul J.M. Smeets^{1,2,3,4}, Kang Rae Cho¹, Ralph G.E. Kempen², Nico A.J.M. Sommerdijk^{2,3*} & James J. De Yoreo^{4*}

¹ Molecular Foundry, Lawrence Berkeley National Laboratory, Berkeley, CA 94720, USA

² Laboratory of Materials and Interface Chemistry and Soft Matter CryoTEM Unit, Eindhoven University of Technology, PO Box 513, 5600 MB Eindhoven, The Netherlands

³ Institute for Complex Molecular Systems, Eindhoven University of Technology, PO Box 513, 5600 MB Eindhoven, The Netherlands

⁴ Physical Sciences Division, Pacific Northwest National Laboratory, Richland, WA 99352, USA

*Correspondence and request for materials should be directed to JJDY and NAJMS,

(james.deyoreo@pnnl.gov; N.Sommerdijk@tue.nl)

The characteristic shapes, structures and properties of biominerals arise from their interplay with a macromolecular matrix^{1,2}. The developing mineral interacts with acidic macromolecules, which are either dissolved in the crystallization medium or associated with insoluble matrix polymers³, that affect growth habits and phase selection or completely inhibit precipitation in solution⁴⁻⁶. Yet little is known about the role of matrix-immobilized acidic macromolecules in directing mineralization. Here, by using *in situ* liquid-phase electron microscopy to visualize the nucleation and growth of CaCO₃ in a matrix of polystyrene sulfonate (PSS), we show that the binding of calcium ions to form Ca-PSS complexes is a key step in the formation of metastable amorphous calcium carbonate (ACC), an important precursor phase in many biomineralization systems⁷. Our findings demonstrate that ion binding can play a significant role in directing nucleation, independently of any control over the free-energy barrier to nucleation.

In many biomineralization systems macromolecular assemblies are thought to present ordered arrays of charged groups, which induce the oriented nucleation of different crystalline phases, often within a matrix or compartment in which the mineral is accumulated prior to crystallization^{8,9}. Here charged biopolymers also play a role in the stabilization of amorphous precursor phases from which many biominerals are formed. This strategy allows the controlled growth of complex shapes and structures without resorting to very slow growth at low levels of supersaturation σ ^{7,10}. Immobilized acidic macromolecules, in particular polysaccharides, also have been suggested to act as concentrators of mineral ions by cation binding prior to crystallization^{11,12}, however, their precise role in controlling biomineralization is still not well understood^{13,14}.

This lack of understanding is, in part, due to the difficulty of studying biomimetic mineralization systems with sufficient spatial and temporal resolution¹⁵. However, liquid phase transmission electron microscopy (LP-TEM) can visualize events *in situ* with high resolution in thin liquid volumes confined within two electron transparent membranes, most often silicon nitride (Si_3N_4)¹⁶. Recent reports showed the nucleation and growth of metal nanoparticles in solution at lattice resolution^{17,18}, the development of metal nanoparticles in the presence of micelles¹⁹, electrochemical precipitation of metallic materials²⁰, as well as iron oxide mineral growth through the oriented attachment of nanoparticles²¹ using video rate imaging. However, the observation of nucleation and growth of inorganic materials within an organic matrix, visualizing both the organic and the inorganic component, has not been reported.

We used a dual inlet flow stage (Supplementary Methods and Materials II, Fig. S1) for *in situ* observation of CaCO_3 nucleation within a macromolecular matrix of the acidic polymer polystyrene sulfonate (PSS). Through imaging and diffraction, we show how the presence of PSS inhibits the crystallization of vaterite (a polymorph of CaCO_3), while promoting the nucleation of ACC, which is confined exclusively to PSS globules. Kinetic data derived from time-lapse series, in combination with calorimetry, spectroscopy and ion-selective electrode measurements show that the negatively charged PSS acts as a sponge that binds calcium ions and locally concentrates them. The localized formation of the metastable ACC results from both the local high supersaturation and interaction with the stabilizing polymer matrix, while the reduced calcium concentration in solution prevents immediate vaterite crystallization outside the globules. Previous mechanistic studies on the role of organic matrices in directing CaCO_3 nucleation using films of model charged organic matrices, focused on the importance of interfacial free energy²² — a parameter determined by crystal-matrix binding that captures the

collective behavior of the system. In contrast, the results presented here demonstrate the important role played by kinetic terms associated with the individual atomistic process of ion binding in directing CaCO_3 nucleation within macromolecular matrices.

To perform the experiments, a 1.25 mM CaCl_2 solution was flowed through the fluid cell, after which carbonate was introduced through in-diffusion of vapor released from the decomposition of solid $(\text{NH}_4)_2\text{CO}_3$ (mainly CO_2 (g) and NH_3 (g)²³) via the second inlet port. Within minutes we observed nucleation of nanoparticles, which were randomly distributed over the Si_3N_4 membranes (Supplementary Video VS1). All particles developed facets (Fig. 1, Supplementary Video VS2) and most displayed a clear diffraction contrast indicating crystallinity. Using electron diffraction, we identified them as vaterite (Fig. 1b&c). In benchtop experiments using Si_3N_4 , vaterite predominated, however some calcite was observed as well. When glass substrates were used we found calcite was produced with this solution composition. Consequently, we assume polymorph selection in PSS-free control experiments in part reflects heterogeneous nucleation on the substrate (Supplementary Data I, Fig. S2,3).

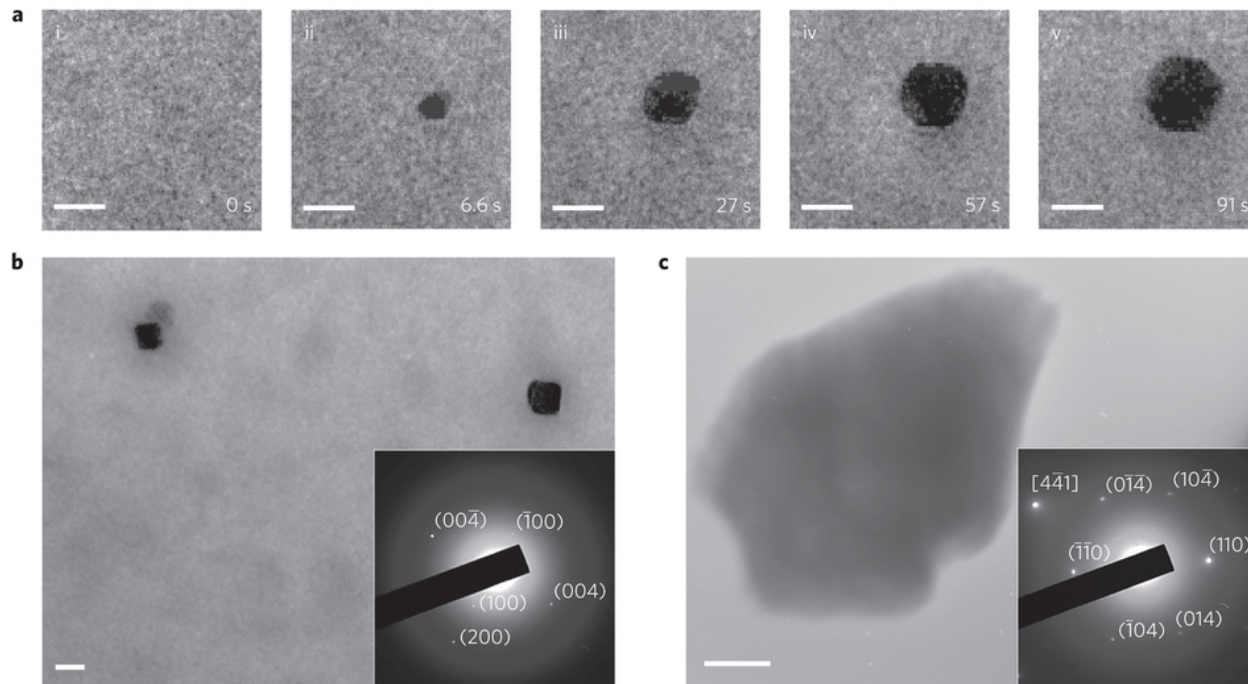


Figure 1 | Rapid vaterite formation in the absence of PSS. **a**, LP-TEM snapshots taken after ~ 5 min of $(\text{NH}_4)_2\text{CO}_3$ diffusion, demonstrating nucleation and growth of a particle in time. $t=0$ s (i) represents the initial imaging time in the view area on the CCD camera (scale bars, 20 nm). **b**, Image of particles in solution (scale bar, 20 nm) with the corresponding electron diffraction pattern (inset) indicating vaterite planes. **c**, A large particle (scale bar, 500 nm) diffracting as a vaterite single crystal with a zone axis in the $[4\bar{4}1]$ direction (inset).

When PSS (7.1×10^{-3} mM) was added to the calcium chloride solution and flowed into the cell, low-contrast objects were observed with diameters of 10 - 100 nm (Fig. 2a, Supplementary video VS3), which were not present in the absence of calcium ions (Supplementary Data III, Fig. S6). The low contrast suggested that these objects were globules of highly hydrated PSS-calcium complexes²⁴, while their static nature implied they were immobilized on the Si_3N_4 -windows of the liquid cell (Fig. 2b). DLS analysis confirmed that the presence of calcium ions induced the

formation of such globules with a size range of 10-100 nm, but with smaller diameters (mode \pm standard deviation: 13 ± 3 nm based on intensity and 8 ± 1 nm based on volume) compared to those measured in TEM (mode \pm standard deviation: 20 ± 3 nm in width) implying that they flattened in contact with the Si_3N_4 window. *In situ* atomic force microscopy (AFM) revealed that when mica surfaces with a surface charge similar to Si_3N_4 (Supplementary Discussion II) were exposed to the polymer-calcium solution, indeed, flattened circular objects formed, which were immobilized on the surface (mode \pm standard deviation 30 ± 3 nm), containing heights of only 0.7 - 2.5 nm and a size range of 10 - 100 nm in width (Fig. 2c, Supplementary Data III, Fig. S4,5,7).

Complexation of the calcium ions with the polymer sulfonate groups was confirmed by the detection of a more positive zeta potential in the presence of calcium ions (Fig. 2e) and by a shift in the asymmetric and symmetric sulfonate stretch vibrations in the Fourier transform infrared (FTIR) spectrum of the PSS (Fig. 2d)²⁵. Calcium ion-selective electrode measurements showed that 56 ± 6 mole % of the total added calcium was bound by the polymer, with a $\text{Ca}^{2+}/\text{SO}_3^-$ ratio of 0.29 ± 0.03 , in agreement with previous results (Supplementary Data IV, Fig. S8)²⁶. This was confirmed by isothermal titration calorimetry which also gave a $\text{Ca}^{2+}/\text{SO}_3^-$ ratio of 0.29, and additionally showed that globule formation is enthalpically-driven (Supplementary Data IV, Fig. S8).

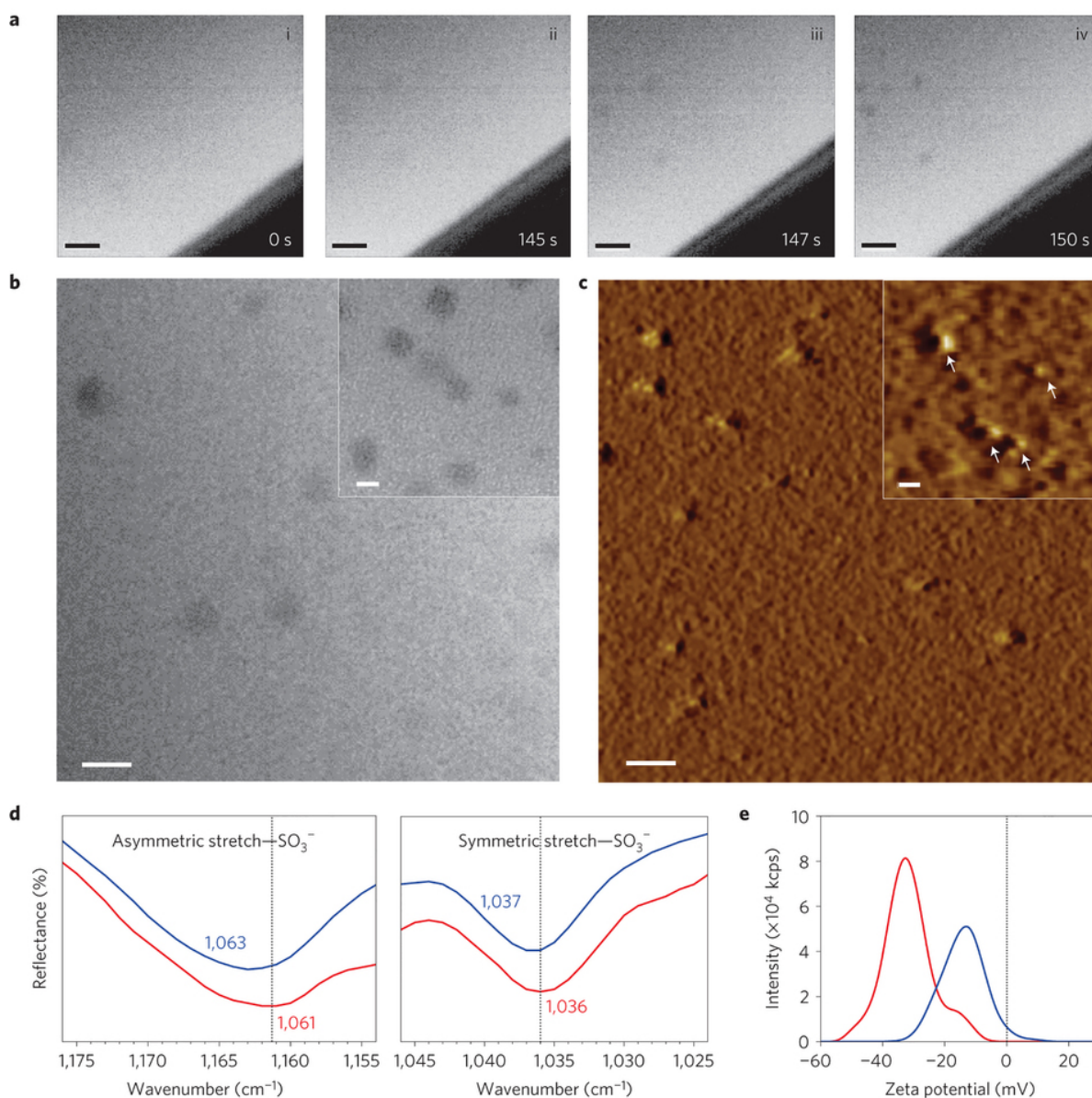


Figure 2 | Analysis of the formation, morphology and chemistry of as-prepared Ca-PSS globules. **a**, LP-TEM snapshots following the formation of Ca-PSS globules on the Si₃N₄ window after the indicated flow time of Ca-PSS solution into the liquid cell: (i) t=0 s (water), (ii) 145 s (iii) 147 s and (iv) 150 s (scale bars, 200 nm). **b,c**, LP-TEM and AFM images, respectively, in liquid, showing large globules (scale bars, 100 nm) and small globules (inset; scale bars, 20 nm; white arrows indicate globules). **d,e**, FTIR spectrum (**d**) of the asymmetric (left) and symmetric (right) stretch of the sulphonate group and zeta potential (**e**) for the Ca-PSS solution (blue) and the solution containing only PSS (red).

The immobilized Ca-PSS globules inside the TEM liquid cell were subsequently exposed to vapor from the decomposition of solid $(\text{NH}_4)_2\text{CO}_3$. After a delay time of ~ 20 min the nucleation of CaCO_3 nanoparticles was observed, growing to sizes of 10-20 nm within seconds (Fig. 3a,c, Supplementary Data V, Fig. S9, Supplementary video VS4&VS5). *In situ* electron diffraction showed that the as-formed particles were amorphous (Fig. 3c, inset, Supplementary Data VI, Fig. S11), but could be converted into calcite (one of the crystalline polymorphs of CaCO_3) upon prolonged exposure to a high intensity electron beam (Supplementary Data VI, Fig. S12, Discussion main text), verifying the nucleated material to be composed of CaCO_3 . Interestingly, ACC nanoparticles were exclusively formed in or on the immobilized Ca-PSS globules, and all ceased growing after tens of seconds. No further precipitation of CaCO_3 was observed outside of the globules, until after ~ 2 hrs of continuous diffusion, when randomly distributed crystals of vaterite appeared (Fig. 3d).

To validate that the observed nucleation of nanoparticles was not the result of the continuous exposure to the electron beam, but solely of the interplay between the carbonate ions and the immobilized Ca-PSS globules, the reaction solution was imaged at different time points between 20 and 65 min using a single exposure with an electron dose of $\sim 50\text{-}300\text{ e}/\text{\AA}^2$, comparable to what is used in low dose cryoTEM imaging²⁷ (see Discussion main text). In these images comparable amorphous nanoparticles were identified, again forming only at the sites of Ca-PSS globules (Supplementary Data VII, Fig. S13). Similarly, when the reaction was allowed to continue for longer periods before the first image was recorded, again randomly distributed vaterite crystals outside of the globules were observed (Fig. 3e,f). Additional benchtop experiments analyzed by AFM, SEM and Raman spectroscopy data confirmed these results for equivalent bulk solutions (Supplementary Data XI, Fig. S16).

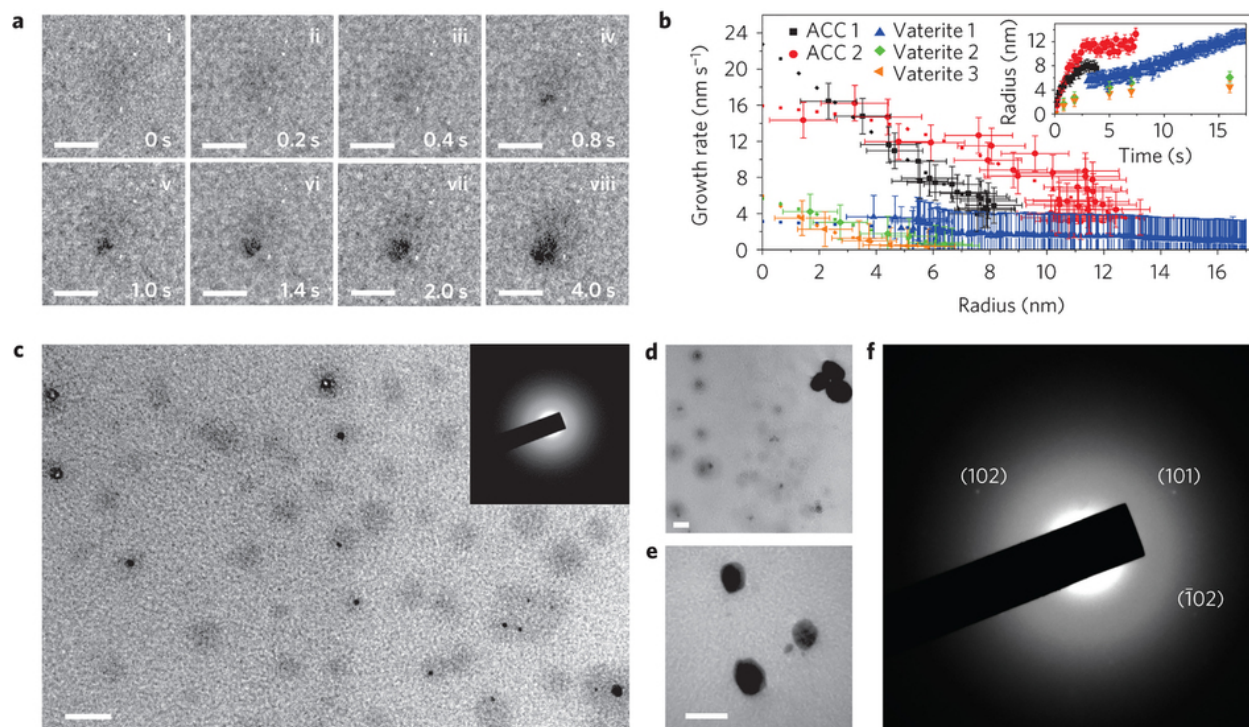


Figure 3 | Nucleation of amorphous calcium carbonate from Ca-PSS globules imaged in LP-TEM. a, Image sequence after 45 min of $(\text{NH}_4)_2\text{CO}_3$ diffusion, showing initial nucleation and growth of a CaCO_3 particle inside or on a primary Ca-PSS globule within 4 s (i–viii) (ACC 1; scale bars, 20 nm). **b,** Extrapolated growth rates versus average radius for two ACC particles (ACC 1 and 2 with PSS) compared against those of three vaterite particles (without PSS) (see Supplementary Methods II, Supplementary Data V, Supplementary Fig. 10 and Supplementary Movie 4 for details on ACC 1, and Supplementary Data V, Supplementary Fig. 9 and Supplementary Movie 5 for details on ACC 2). A logarithmic function is used to fit each set of data points and to extrapolate to zero radius. Inset: Measured radius versus time for the ACC (see Supplementary Table 1) and vaterite particles. **c,** Lower-magnification image (scale bar, 50 nm) exhibiting many nuclei in Ca-PSS globules and an electron diffraction pattern (inset) showing that they are amorphous (Supplementary Data VI and Supplementary Fig. 11). Differences in the radial distribution of black and white contrast in the nucleated ACC particles are due to differences in the

location relative to the focal plane: black signifies a near-focus condition (near the bottom Si_3N_4 membrane) and white signifies over-focus (near the top membrane); see also Supplementary Data V. Therefore, one can distinguish nucleated ACC in (or near) a globule that is adsorbed on the top or bottom Si_3N_4 membrane of the liquid cell. **d**, Image after ~ 2 h of $(\text{NH}_4)_2\text{CO}_3$ diffusion, showing large particles (upper right corner) exhibiting diffraction contrast contours that have nucleated and grown in the vicinity of the ACC particles formed from the Ca-PSS globules (scale bar, 50 nm). **e**, Control reaction after ~ 2 h of diffusion without previous beam exposure, eliminating the influence of the beam on particle formation (scale bar, 50 nm). **f**, Diffraction pattern of particles in **e**, showing spots of the (101) and (102) planes characteristic of vaterite.

Growth rate profiles of ACC and vaterite were extracted from the time-lapse series recorded for the precipitation of CaCO_3 in the presence and absence of PSS, respectively (for details, see Supplementary Methods and Materials II, Supplementary Data V, Fig. S10). The initial growth rates — determined by extrapolation of the profiles to zero radius R — were higher for the ACC particles formed in the presence of PSS (16-23 nm/s) than for the vaterite crystallites formed in its absence (3-6 nm/s) (Fig. 3b). These initial growth rates are directly related to the value of σ at the time of nucleation and can be used to estimate its value (see Supplementary Data IX for details). Two approximations permit this. First, because ACC is amorphous, the surface is expected to be atomically rough and so every site serves as a potential attachment — or “kink” — site. Similarly, for vaterite the high curvature at the time of nucleation allows us to make the same approximation. Second, at moderate to high values of σ , the net addition of ions to a kink site is dominated by attachment events, which are in turn controlled by ion desolvation rates and these should be similar for all CaCO_3 phases as they are primarily a property of the solution²⁸.

Taking the known dependence of step speed on σ for calcite and an initial radial growth speed of 16-23 nm/s, we estimate ACC nucleation to occur at $\sigma = 1.0 - 1.8$ *relative to ACC* in the presence of PSS and vaterite nucleation to occur at $\sigma = 0.5 - 0.6$ *relative to vaterite* in its absence (Supplementary Data VIII). Because we would expect ACC nucleation to be more likely than vaterite nucleation at equal supersaturation based on ACC's lower surface energy^{28,29}, these results show that the addition of PSS significantly inhibits ACC nucleation. This inhibition also leads to a significant difference in $\text{Ca}^{2+} : \text{CO}_3^{2-}$ ratios. For an initial Ca^{2+} concentration of 1.25 mM, and 56 mole % of the calcium bound in the PSS globules, we estimate these values of σ to correspond to a $\text{Ca}^{2+} : \text{CO}_3^{2-}$ ratio of 1 : 2 – 1 : 5 and 1 : 0.013 – 1 : 0.014 during the ACC and vaterite nucleation events, respectively (Supplementary Data X).

The data also shows that the growth rates of individual vaterite particles are very similar, while there is some variation in the ACC growth rates. This implies that in the absence of the PSS the concentrations of Ca^{2+} and CO_3^{2-} are similar throughout the imaging area, but that the Ca^{2+} concentration varies slightly between individual globules.

We can understand the buildup of high supersaturation levels in Ca-PSS globules and the consequent localized nucleation of the ACC as follows. Initially, the negatively charged polymer sequesters the calcium ions, thus lowering the calcium concentration in solution and preventing nucleation outside the polymer containing areas. The polymer additionally stabilizes the amorphous phase, leading to ACC nucleation only at the sites of the globules. With the continued generation of carbonate via CO_2 influx, the solution outside of the globules eventually reaches sufficiently high supersaturation to nucleate the vaterite.

The cessation of ACC nanoparticle growth suggests the calcium ions bound within the Ca-PSS globules provided the cation supply and that growth stopped when these ions were depleted to the solubility limit of ACC. Indeed, taking into account that the Ca^{2+} concentration in solution is significantly reduced due to the initial binding with PSS, there will be little or no gradient to drive the diffusion of calcium ions towards the growing mineral particles inside the polymer globules. We have schematically summarized our findings in Fig. 4.

The scenario presented in Fig. 4 is not a consequence of specific features associated with LP-TEM, which has some known limitations³⁰⁻³⁴, e.g. the interaction of the electron beam with the fluid is a matter of concern, as it may induce gradients in pH due to water decomposition, and generate beam induced deposition of nanoparticles³⁵. However, in contrast to cryo-TEM, where electron damage is cumulative, LP-TEM allows recovery of structures and their liquid environment via chemical equilibration. Hence, there should be a threshold dose rate at which beam damage and recovery balance will be practically undisturbed^{36,37}.

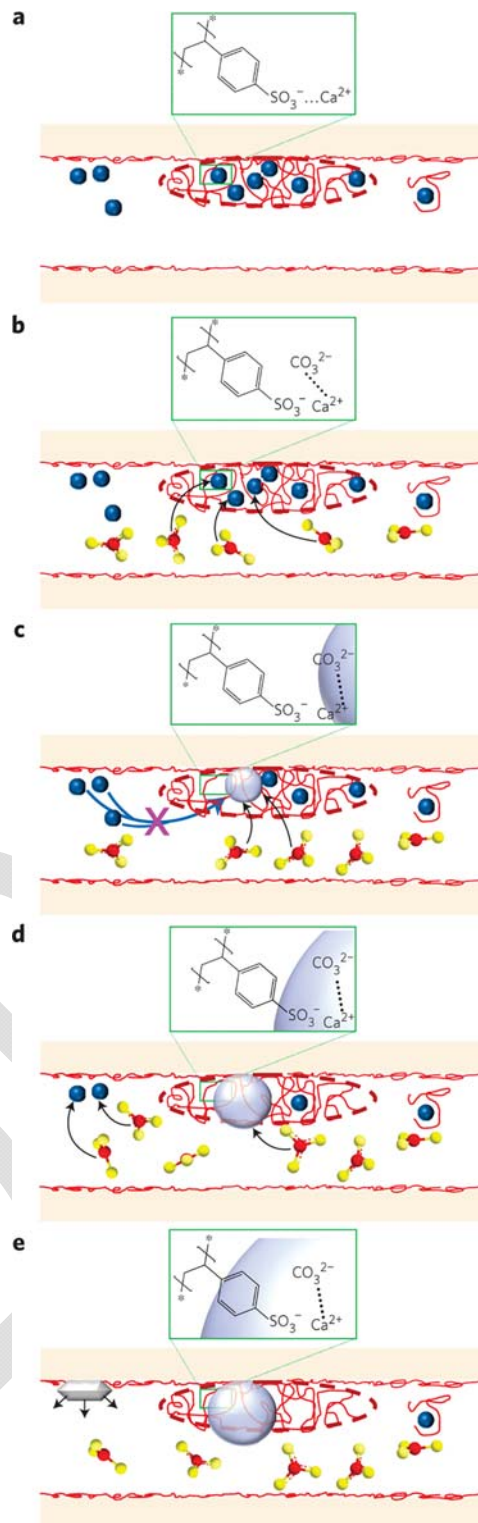


Figure 4 | Mechanism of CaCO_3 mineral formation in the biomimetic matrix. a, Initially, Ca^{2+} (blue dots) binds with the SO_3^- – group of the PSS (red), as indicated in molecular detail in the green box,

leading to a locally high Ca^{2+} concentration in the Ca-PSS globules deposited on the surface of the Si_3N_4 window (orange) and to low free Ca^{2+} concentration in the surrounding solution, where dissolved PSS is also bound to Ca^{2+} . **b**, CO_3^{2-} (red and yellow dots) from the ammonium carbonate source then diffuses into the globules (black arrows), where it binds with Ca^{2+} , replacing the weaker $\text{SO}_3^-/\text{Ca}^{2+}$ interaction and creating a supersaturated state. **c**, At a critical value of supersaturation (after ~ 20 min), ACC nuclei (light blue sphere) appear and grow as a result of the continued generation of CO_3^{2-} . However, free Ca^{2+} does not diffuse into the globules (blue arrows with pink cross) owing to the low Ca^{2+} concentration in solution compared with that in the globules, which is fixed by the solubility of ACC. **d**, The growth of ACC stops when the supply of excess Ca^{2+} ions in the globules is depleted, but the continuous generation of CO_3^{2-} eventually raises the supersaturation of the solution to the level required for vaterite nucleation on the Si_3N_4 window. **e**, Vaterite continues to grow until the remaining free Ca^{2+} has been depleted.

We determined the electron dose rate at our nominal conditions to be $1 \pm 0.5 \times 10^3$ electrons $\text{\AA}^{-2} \text{ s}^{-1}$, for our measurements using a blank stage. To exclude the possibility that our observations would be the result of the interaction of the electron beam with the sample solution, we recorded low dose control images by applying a single exposure to pristine areas not previously illuminated by the electron beam. We did this for both our measurements of ACC formation in or on Ca-PSS globules (Supplementary Data VII, Fig. S13) and vaterite growth with PSS outside of globules (Fig. 3e,f). Acquisition times of 0.1 or 0.2 seconds were used, yielding electron doses of $\sim 50\text{-}300 \text{ e}/\text{\AA}^2$, which are comparable to those reliably used in low dose cryo-TEM imaging²⁷. Thus, this indicates that under the appropriate conditions LP-TEM can be reliably used for the artifact free imaging of electron sensitive materials.

Due to the large dimensions of the fluid cell relative to both the expected thickness of hydration layers and critical nucleus size, we do not expect confinement effects to be manifest in the nucleation rates or pathways. The separate effects of small volume on extending the lifetime of ACC by limiting the likelihood of replacement by more stable crystalline phases, as observed in other studies^{38,39}, are not a factor in the cell configuration used here as demonstrated by a previous study using the same cell geometry⁴⁰ (See Supplementary Discussion I for details).

The results presented here have a clear parallel in biomineralization, supporting the model Addadi et al. proposed for the action of sulfated carbohydrates that surround the nucleation sites for the aragonitic tablets in the nacreous layer of mollusk shells^{11,13}. In this model, the strong calcium binding capacity of the sulfates generates the high local supersaturation required for mineral nucleation. As the oriented nucleation of the mineral is thought to occur on the co-immobilized β -sheet protein structure, the authors suggest that the calcium ions are collected without being bound to specific groups. Our present results show that the immobilized PSS is a functional mimic of the sulfated carbohydrates in the natural system and indeed is an effective concentrator for calcium, locally increasing the supersaturation such that nucleation can occur. However, our data also shows that specific binding occurs with the polymer sulfonate groups, which subsequently leads to the localized nucleation of ACC. Moreover, the data indicate that nucleation is restricted to the immobilized PSS and is not induced by solvated PSS chains in solution, although some interaction of these polymers with the developing mineral cannot be ruled out.

Our results contrast with findings from recent *in situ* optical and AFM studies of calcite nucleation on model matrices consisting of alkylthiol SAMs and polysaccharide films, both of which were also negatively charged^{22,29}. Analysis of the nucleation data in both cases showed

that the films significantly decreased the interfacial energy that determines the free energy barrier to nucleation. Force spectroscopy measurements then revealed the direct relationship between the interfacial energy controlling nucleation and the strength of the film-crystal binding free energy. However, although the probability of nucleation scales exponentially with the free energy barrier, it also scales exponentially with a kinetic barrier associated with atomistic processes like ion desolvation and binding. No insights into the effects on the kinetic barrier were obtained from these previous studies. The findings presented here now reveal the significant role that ion binding can play in directing nucleation independent of any controls over the free energy barriers.

Methods Summary

Detailed information on the following methods can be found in the Supplementary Methods and Materials: Synthesis of Ca-PSS globules and CaCO₃ formation, Transmission Electron Microscopy, Atomic Force Microscopy, Fourier Transform Infrared Microscopy, Isothermal Titration Calorimetry, Dynamic Light Scattering and Zeta Potential Measurements, Scanning Electron Microscopy, Confocal Raman Microscopy and Ion Selective Electrode Experiments.

References

- 1 Lowenstam, H. A. & Weiner, S. *On Biomineralization*. (Oxford University Press, 1989).
- 2 Mann, S. *Biomineralization, Principles and Concepts in Bioinorganic Materials Chemistry*. (Oxford University Press, 2001).
- 3 Special issue on Biomineralization. *Chemical reviews* **108**, 4329-4978 (2008).
- 4 Sommerdijk, N. & de With, G. Biomimetic CaCO₃ Mineralization using Designer Molecules and Interfaces. *Chemical Reviews* **108**, 4499-4550, doi:10.1021/cr078259o (2008).

- 5 Meldrum, F. C. & Colfen, H. Controlling Mineral Morphologies and Structures in Biological and Synthetic Systems. *Chemical Reviews* **108**, 4332-4432, doi:10.1021/cr8002856 (2008).
- 6 Gower, L. B. Biomimetic Model Systems for Investigating the Amorphous Precursor Pathway and Its Role in Biomineralization. *Chemical Reviews* **108**, 4551-4627, doi:10.1021/cr800443h (2008).
- 7 Addadi, L., Raz, S. & Weiner, S. Taking advantage of disorder: Amorphous calcium carbonate and its roles in biomineralization. *Advanced Materials* **15**, 959-970, doi:10.1002/adma.200300381 (2003).
- 8 Nudelman, F., Chen, H. H., Goldberg, H. A., Weiner, S. & Addadi, L. Spiers memorial lecture: Lessons from biomineralization: comparing the growth strategies of mollusc shell prismatic and nacreous layers in *Atrina rigida*. *Faraday Discussions* **136**, 9-25, doi:10.1039/b704418f (2007).
- 9 Young, J. R., Davis, S. A., Bown, P. R. & Mann, S. Coccolith ultrastructure and biomineralisation. *Journal of Structural Biology* **126**, 195-215 (1999).
- 10 Olszta, M. J. *et al.* Bone structure and formation: A new perspective. *Materials Science & Engineering R-Reports* **58**, 77-116, doi:10.1016/j.mser.2007.05.001 (2007).
- 11 Addadi, L., Moradian, J., Shay, E., Maroudas, N. G. & Weiner, S. A CHEMICAL-MODEL FOR THE COOPERATION OF SULFATES AND CARBOXYLATES IN CALCITE CRYSTAL NUCLEATION - RELEVANCE TO BIOMINERALIZATION. *Proceedings of the National Academy of Sciences of the United States of America* **84**, 2732-2736, doi:10.1073/pnas.84.9.2732 (1987).
- 12 Marsh, M. E. POLYANION-MEDIATED MINERALIZATION - ASSEMBLY AND REORGANIZATION OF ACIDIC POLYSACCHARIDES IN THE GOLGI SYSTEM OF A COCCOLITHOPHORID ALGA DURING MINERAL DEPOSITION. *Protoplasma* **177**, 108-122, doi:10.1007/bf01378985 (1994).
- 13 Nudelman, F., Gotliv, B. A., Addadi, L. & Weiner, S. Mollusk shell formation: Mapping the distribution of organic matrix components underlying a single aragonitic tablet in nacre. *Journal of Structural Biology* **153**, 176-187, doi:10.1016/j.jsb.2005.09.009 (2006).
- 14 Marsh, M. E., Ridall, A. L., Azadi, P. & Duke, P. J. Galacturonomannan and Golgi-derived membrane linked to growth and shaping of biogenic calcite. *Journal of structural biology* **139**, 39-45, doi:10.1016/s1047-8477(02)00503-8 (2002).
- 15 Dey, A., de With, G. & Sommerdijk, N. A. J. M. In situ techniques in biomimetic mineralization studies of calcium carbonate. *Chemical Society Reviews* **39**, 397-409, doi:10.1039/b811842f (2010).
- 16 de Jonge, N. & Ross, F. M. Electron microscopy of specimens in liquid. *Nature Nanotechnology* **6**, 695-704, doi:10.1038/nnano.2011.161 (2011).
- 17 Liao, H. G., Cui, L. K., Whitlam, S. & Zheng, H. M. Real-Time Imaging of Pt₃Fe Nanorod Growth in Solution. *Science* **336**, 1011-1014, doi:10.1126/science.1219185 (2012).
- 18 Yuk, J. M. *et al.* High-Resolution EM of Colloidal Nanocrystal Growth Using Graphene Liquid Cells. *Science* **336**, 61-64, doi:10.1126/science.1217654 (2012).
- 19 Parent, L. R. *et al.* Direct in Situ Observation of Nanoparticle Synthesis in a Liquid Crystal Surfactant Template. *ACS Nano* **6**, 3589-3596, doi:10.1021/nn300671g (2012).
- 20 Radisic, A., Vereecken, P. M., Hannon, J. B., Searson, P. C. & Ross, F. M. Quantifying Electrochemical Nucleation and Growth of Nanoscale Clusters Using Real-Time Kinetic Data. *Nano Letters* **6**, 238-242, doi:10.1021/nl052175i (2006).
- 21 Li, D. *et al.* Direction-Specific Interactions Control Crystal Growth by Oriented Attachment. *Science* **336**, 1014-1018 (2012).
- 22 Giuffre, A. J., Hamm, L. M., Han, N., De Yoreo, J. J. & Dove, P. M. Polysaccharide chemistry regulates kinetics of calcite nucleation through competition of interfacial energies. *Proceedings of the National Academy of Sciences*, doi:10.1073/pnas.1222162110 (2013).

- 23 Ihli, J., Bots, P., Kulak, A., Benning, L. G. & Meldrum, F. C. Elucidating Mechanisms of Diffusion-Based Calcium Carbonate Synthesis Leads to Controlled Mesocrystal Formation. *Advanced Functional Materials*, 1965-1973, doi:10.1002/adfm.201201742 (2012).
- 24 Trotsenko, O., Roiter, Y. & Minko, S. Conformational Transitions of Flexible Hydrophobic Polyelectrolytes in Solutions of Monovalent and Multivalent Salts and Their Mixtures. *Langmuir* **28**, 6037-6044 (2012).
- 25 Wang, T., Zhao, C., Xu, J. & Sun, D. Enhanced Ca²⁺ binding with sulfonic acid type polymers at increased temperatures. *Colloids and Surfaces A: Physicochemical and Engineering Aspects* **417**, 256-263 (2013).
- 26 Verch, A., Gebauer, D., Antonietti, M. & Colfen, H. How to control the scaling of CaCO₃: a "fingerprinting technique" to classify additives. *Physical Chemistry Chemical Physics* **13**, 16811-16820, doi:10.1039/c1cp21328h (2011).
- 27 Friedrich, H., Frederik, P. M., de With, G. & Sommerdijk, N. A. J. M. Imaging of Self-Assembled Structures: Interpretation of TEM and Cryo-TEM Images. *Angewandte Chemie International Edition* **49**, 7850-7858, doi:10.1002/anie.201001493 (2010).
- 28 De Yoreo, J. J. & Vekilov, P. G. in *Reviews in Mineralogy and Geochemistry* Vol. 54 57-93 (2003).
- 29 Hamm, L. M. *et al.* Reconciling disparate views of template-directed nucleation through measurement of calcite nucleation kinetics and binding energies. *Proceedings of the National Academy of Sciences* **111**, 1304-1309, doi:10.1073/pnas.1312369111 (2014).
- 30 de Jonge, N. & Ross, F. M. Electron microscopy of specimens in liquid. *Nat Nano* **6**, 695-704 (2011).
- 31 Browning, N. D. *et al.* Recent developments in dynamic transmission electron microscopy. *Current Opinion in Solid State and Materials Science* **16**, 23-30, doi:http://dx.doi.org/10.1016/j.cossms.2011.07.001 (2012).
- 32 Evans, J. E., Jungjohann, K. L., Browning, N. D. & Arslan, I. Controlled Growth of Nanoparticles from Solution with In Situ Liquid Transmission Electron Microscopy. *Nano Letters* **11**, 2809-2813, doi:10.1021/nl201166k (2011).
- 33 Woehl, T. J. *et al.* Experimental procedures to mitigate electron beam induced artifacts during in situ fluid imaging of nanomaterials. *Ultramicroscopy* **127**, 53-63, doi:http://dx.doi.org/10.1016/j.ultramic.2012.07.018 (2013).
- 34 Noh, K. W., Liu, Y., Sun, L. & Dillon, S. J. Challenges associated with in-situ TEM in environmental systems: The case of silver in aqueous solutions. *Ultramicroscopy* **116**, 34-38, doi:http://dx.doi.org/10.1016/j.ultramic.2012.03.012 (2012).
- 35 van de Put, M. W. P. *et al.* Writing Silica Structures in Liquid with Scanning Transmission Electron Microscopy. *Small*, doi:10.1002/sml.201400913 (2014).
- 36 Karuppasamy, M., Karimi Nejadasl, F., Vulovic, M., Koster, A. J. & Ravelli, R. B. G. Radiation damage in single-particle cryo-electron microscopy: effects of dose and dose rate. *Journal of Synchrotron Radiation* **18**, 398-412, doi:doi:10.1107/S090904951100820X (2011).
- 37 Jungjohann, K. L., Evans, J. E., Aguiar, J. A., Arslan, I. & Browning, N. D. Atomic-Scale Imaging and Spectroscopy for In Situ Liquid Scanning Transmission Electron Microscopy. *Microscopy and Microanalysis* **18**, 621-627, doi:doi:10.1017/S1431927612000104 (2012).
- 38 Stephens, C. J., Ladden, S. F., Meldrum, F. C. & Christenson, H. K. Amorphous Calcium Carbonate is Stabilized in Confinement. *Advanced Functional Materials* **20**, 2108-2115, doi:10.1002/adfm.201000248 (2010).
- 39 Tester, C. C. *et al.* In vitro synthesis and stabilization of amorphous calcium carbonate (ACC) nanoparticles within liposomes. *CrystEngComm* **13**, 3975-3978, doi:10.1039/c1ce05153a (2011).

40 Nielsen, M. H., Aloni, S. & De Yoreo, J. J. In situ TEM imaging of CaCO₃ nucleation reveals coexistence of direct and indirect pathways. *Science* **345**, 1158-1162, doi:10.1126/science.1254051 (2014).

Acknowledgements

We thank V. Altoe and S. Aloni for the use of, and assistance with the JEOL-2100F, J. Tao for the help with Confocal Raman Microscopy, H. Friedrich and M. Nielsen for help with TEM data analysis. This research was supported by the U.S. Department of Energy, Office of Basic Energy Sciences, at Lawrence Berkeley National Laboratory, and at the Pacific Northwest National Laboratory (PNNL). Characterization of PSS globule formation was supported by the Materials Science and Engineering Division. Investigation of calcium carbonate nucleation was supported by the Division of Chemical Sciences, Geosciences, and Biosciences. Transmission electron microscopy was performed at the Molecular Foundry, Lawrence Berkeley National Laboratory, which is supported by the Office of Basic Energy Sciences, Scientific User Facilities Division. PNNL is operated by Battelle for the U.S. Department of energy under Contract DE-AC05-76RL01830. The work of P.J.M.S. and N.A.J.M.S. is supported by a VICI grant of the Dutch Science Foundation, NWO, The Netherlands.

Author Contributions

P.J.M.S. carried out most experiments and co-wrote the manuscript. K.R.C. provided expertise and support in the AFM measurements. P.J.M.S. and J.J.D.Y. performed the growth rate and diffusion analysis. R.G.E.K. contributed to developing and utilizing the MATLAB procedure for

growth rate determinations. N.A.J.M.S. and J.J.D.Y. designed the research and co-wrote the manuscript. All authors discussed the results and revised the manuscript.

Competing Financial Interest statement

The authors declare no competing financial interests.

DRAFT